

SPIRIT: Short-term Prediction of solar IRradlance for zero-shot Transfer learning using Foundation Models

Aditya Mishra*
International Institute of Information
Technology, Hyderabad
India
aditya.mishra@students.iit.ac.in

T Ravindra*
International Institute of Information
Technology, Hyderabad
India
t.ravindra@students.iit.ac.in

Srinivasan Iyengar
Microsoft Corporation
India
sriyengar@microsoft.com

Shivkumar Kalyanaraman
Microsoft Corporation
India
shkalya@microsoft.com

Ponnuram Kumaraguru
International Institute of Information
Technology, Hyderabad
India
pk.guru@iiit.ac.in

ABSTRACT

Traditional solar forecasting models are based on several years of site-specific historical irradiance data, often spanning five or more years, which are unavailable for newer photovoltaic farms. As renewable energy is highly intermittent, building accurate solar irradiance forecasting systems is essential for efficient grid management and enabling the ongoing proliferation of solar energy, which is crucial to achieve the United Nations' net zero goals. In this work, we propose SPIRIT, a novel approach leveraging foundation models for solar irradiance forecasting, making it applicable to newer solar installations. Our approach outperforms state-of-the-art models in zero-shot transfer learning by about 70%, enabling effective performance at new locations without relying on any historical data. Further improvements in performance are achieved through fine-tuning, as more location-specific data becomes available. These findings are supported by statistical significance, further validating our approach. SPIRIT represents a pivotal step towards rapid, scalable, and adaptable solar forecasting solutions, advancing the integration of renewable energy into global power systems.

CCS CONCEPTS

• **Computing methodologies** → **Machine learning**: Foundation models; Transfer learning; • **Applied computing** → *Forecasting*; • **Hardware** → *Renewable energy*.

KEYWORDS

Solar Forecasting, Renewable Energy, Foundation Models, Transfer Learning, Zero-shot Learning, Fine-tuning, Deep Learning

*Equal contribution.

Permission to make digital or hard copies of all or part of this work for personal or classroom use is granted without fee provided that copies are not made or distributed for profit or commercial advantage and that copies bear this notice and the full citation on the first page. Copyrights for components of this work owned by others than the author(s) must be honored. Abstracting with credit is permitted. To copy otherwise, or republish, to post on servers or to redistribute to lists, requires prior specific permission and/or a fee. Request permissions from permissions@acm.org.
KDD'25, 978-1-4503-XXXX-X/18/06

© 2025 Copyright held by the owner/author(s). Publication rights licensed to ACM.
ACM ISBN 978-x-xxxx-xxxx-x/YY/MM. . . \$15.00
<https://doi.org/XXXXXXXX.XXXXXXX>

ACM Reference Format:

Aditya Mishra, T Ravindra, Srinivasan Iyengar, Shivkumar Kalyanaraman, and Ponnuram Kumaraguru. 2025. SPIRIT: Short-term Prediction of solar IRradlance for zero-shot Transfer learning using Foundation Models. In *Proceedings of Make sure to enter the correct conference title from your rights confirmation email (KDD'25)*. ACM, New York, NY, USA, 13 pages. <https://doi.org/XXXXXXXX.XXXXXXX>

1 INTRODUCTION

The proliferation of solar energy is paramount for electrification and the global energy transition to meet the Net Zero commitments of the United Nations [40]. As the world moves toward renewable sources, solar energy is notable for its accessibility and potential to significantly reduce carbon emissions [43]. Expanding the solar energy infrastructure is crucial to mitigate the effects of climate change [7] and meet the energy demands arising from sectors such as data centers [3], transportation [27], and buildings [21].

Unlike conventional power sources such as thermal and nuclear, solar energy has inherent shortcomings. Its intermittency, due to the daily and seasonal variations in sunlight, poses significant challenges for energy grid stability [2]. One notable issue arising from the higher penetration of solar power is the “duck curve” [19], where the mismatch between solar energy production and peak energy demand leads to significant challenges in grid management. Although storage capacity is increasing, electricity grids typically operate as a *just-in-time* system where energy supply and demand must be balanced [23]. To ensure grid efficiency, renewable operators must pay a deviation penalty to discourage unplanned energy contributions, thereby maintaining a balanced and predictable energy supply [49]. Thus, accurate short-term solar predictions are crucial for the efficient operation of the energy grid [20].

Existing approaches for short-term forecasting use Sky Cameras — i.e., a fish-eye lens camera positioned to look directly towards the zenith — which require extensive site-specific data to train models [14, 15]. These models have demonstrated the ability to develop high-accuracy models, albeit using training data spanning multiple years. With the overall solar PV fleet expected to increase from 1 TW in 2022 to 10 TW by 2030 [1], 90% of the solar farms worldwide will have negligible data to train custom models from scratch. Thus,

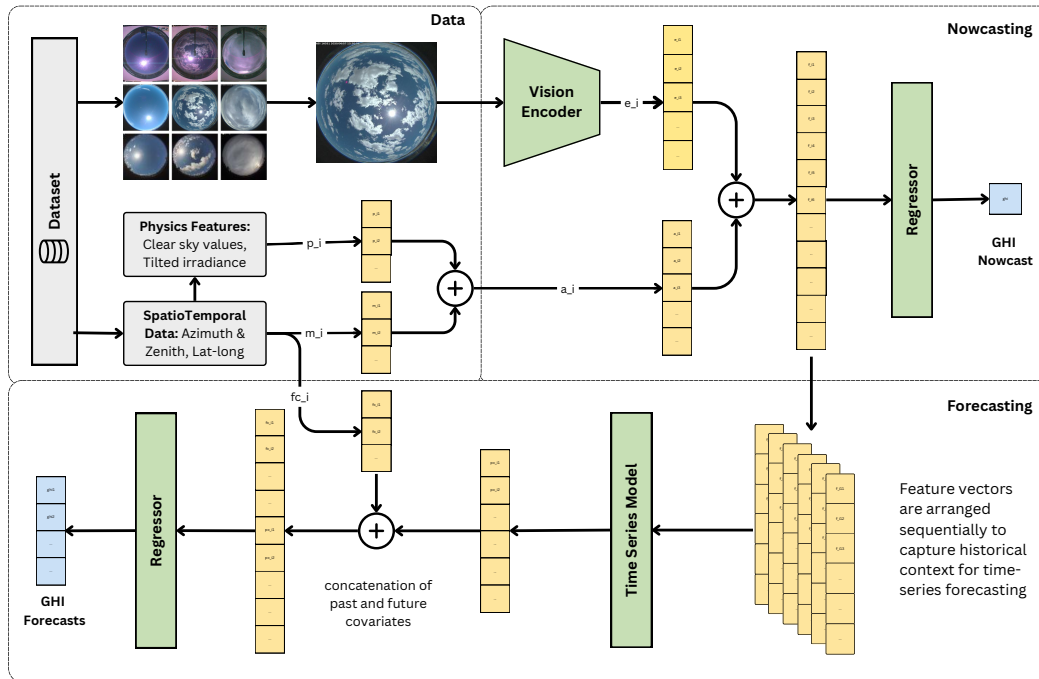


Figure 1: Illustration of our system: A vision encoder (top-left) extracts embeddings from a sky camera image sampled from a diverse set spanning multiple locations and setups. Physics-inspired features are derived and integrated with auxiliary values, then merged with the image embedding (top-middle) into a unified representation. For nowcasting (right), a regressor predicts Global Horizontal Irradiance from this feature vector. For forecasting (bottom), a time-series model processes past feature vectors to create a context embedding, which is concatenated with a future covariate vector—constructed from known future values—to form the final latent representation. A regressor then maps this representation to future GHI values (bottom-right).

lack of sufficient site-specific solar data underscores the need for approaches that do not compromise model performance.

With the advent of vision foundation models, we have seen improvement in accuracy of various Computer Vision tasks — such as feature extraction, object detection, etc. — using zero-shot and few-shot approaches (i.e., with limited or no custom training data) [11, 22, 51]. In addition, physics-inspired feature engineering has significantly improved model performance by incorporating domain-specific knowledge, leading to more accurate and interpretable predictions in real-world problems [12, 34]. In this work, our hypothesis is as follows: *Can we leverage state-of-the-art vision foundation models and physics-inspired features, along with transfer learning strategies, to reduce the dependence on site-specific sky camera imagery data?*

To address these challenges, we introduce SPIRIT, a novel approach to solar irradiance forecasting with an inductive bias toward enhanced generalizability. In designing, implementing, and evaluating our approach, we make the following contributions:

(1) We develop a novel system that leverages foundation models and physics-informed features, eliminating the need for site-specific model training while enabling effective adaptation across diverse

transfer learning scenarios. The flexibility of our framework ensures seamless integration of future advancements in vision models without requiring significant architectural modifications.

(2) Motivated by real-world deployment constraints, we demonstrate that SPIRIT can rapidly scale to new solar plant locations without prior sky camera data, significantly accelerating integration into operational workflows.

2 RELATED WORK

Traditional methods for solar forecasting have relied heavily on Numerical Weather Prediction (NWP) models and satellite imagery [29]. While these methods provide valuable insights, they often lack the spatial and temporal resolution required for accurate short-term forecasts. For instance, NWP models typically operate on a grid scale of several kilometers and update every few hours which may not capture rapid changes in cloud cover that affect solar irradiance [24]. Over the past few years, several time series forecasting approaches have been used for solar forecasting. However, they typically operate on a time frame of multiple hours to day-ahead and are not suitable for capturing short-term variations in solar generation due to transient factors such as cloud cover [13, 20].

Use of sky camera imagers for short-term solar forecasting has garnered significant attention in recent years due to their potential to enhance the accuracy of solar power predictions [14, 15, 33]. Sky cameras, equipped with fish-eye lenses, capture wide-angle images of the sky, providing valuable data on cloud cover and movement, which are critical factors in solar irradiance forecasting [10]. Recent advancements have focused on leveraging sky cameras to address the limitations of traditional approaches. Hammond et al. [15] and Gao et al. [14] demonstrated the potential of sky cameras in developing high-accuracy models for short-term solar forecasting. These studies utilized extensive site-specific data collected over multiple years to train their models, achieving significant improvements in forecast accuracy compared to traditional methods.

Siddiqui et al. [44] proposed a deep learning framework using sky-camera images and auxiliary meteorological data to predict solar irradiance. Their approach employs a convolutional neural network (CNN) with dilated convolutions, followed by an LSTM for temporal forecasting up to four hours ahead. By training on 10 years of data, they demonstrated that incorporating auxiliary data such as temperature, wind speed, and relative humidity enhances generalization and stability in predictions. Similarly, Gao et al. [14] introduced a transformer-based architecture that integrates a clear sky model to estimate the residual irradiance beyond clear-sky assumptions. Trained on 10 years of data, their model achieves improved forecasting accuracy compared to earlier CNN-LSTM-based methods. Both works underscore the importance of leveraging sky images and auxiliary data for precise solar nowcasting and forecasting. Despite their promise, sky camera-based approaches face challenges related to data availability. With the global solar PV fleet expected to increase from 1 TW in 2022 to 10 TW by 2030, a large majority of the solar farms worldwide will have negligible historical data to train custom models from scratch.

Building upon these challenges, it becomes evident that addressing the limited availability of site-specific data is critical for advancing solar forecasting. Although the use of sky cameras and auxiliary data has substantially improved short-term predictions, the scalability of these methods remains constrained by the dearth of historical data at many solar installations. In this context, transfer learning emerges as a promising solution, as it enables the leveraging of knowledge from pre-trained models and the adaptation of learned representations across different datasets and locations. Notably, previous work such as Nie *et al.* [33] has demonstrated that training on a fusion of multiple datasets yields models that perform better on each individual dataset, thereby highlighting the potential benefits of cross-dataset knowledge transfer.

3 SPIRIT DESIGN

3.1 Key Concepts and Problem Setup

Nowcasting refers to the prediction of solar power generation over very short time horizons, typically ranging from a few minutes to a few hours [26]. In contrast, short-term forecasting extends the prediction horizon to cover periods from one hour to 24 hours [39]. Methods developed to provide forecasts utilize various data sources, such as satellite data [26, 28], weather station observations [26], and sky camera images [14, 44, 48]. Nowcasting and short-term forecasting are indispensable for managing the intermittency of

solar power, allowing grid operators to perform better scheduling, dispatching, and balancing of energy resources [6, 8].

Sky Camera: Sky cameras enhance nowcasting and short-term forecasting by capturing sky images with fish-eye lenses, providing detailed cloud movement, and sun position data. These images enable algorithms to track cloud dynamics and predict their trajectories, essential for estimating solar irradiance [10, 41]. Offering a low-latency alternative to weather satellites, sky cameras facilitate real-time monitoring. However, variations in camera setup and quality affect image appearance, as shown in Figure 4 in Appendix A.1. As a key tool in solar forecasting, sky cameras contribute to more reliable energy predictions [37]. Further details are provided in Appendix B.

Irradiance measurements: Understanding solar irradiance requires distinguishing between three key measurements:

(1) **Direct Normal Irradiance (DNI):** The amount of solar radiation received per unit area on a surface perpendicular to the sun's rays without being scattered or diffused by the atmosphere.

(2) **Diffuse Horizontal Irradiance (DHI):** The portion of solar radiation that reaches a horizontal surface after being scattered by molecules, aerosols, and clouds in the atmosphere. Unlike DNI, DHI comes from all directions in the sky and plays a crucial role during overcast conditions when direct sunlight is obstructed.

(3) **Global Horizontal Irradiance (GHI):** The total solar radiation received on a horizontal surface, combining both direct and diffuse components. GHI is the sum of DNI, projected onto a horizontal plane, and DHI:

$$GHI = DNI \times \cos(\theta) + DHI \quad (1)$$

where θ is the angle between the direction of incoming solar radiation and the vertical, called the zenith angle.

GHI is the most commonly used irradiance measure in solar energy applications, as it directly influences photovoltaic (PV) panel performance and solar power generation, making it the primary focus of research in irradiance forecasting. Henceforth, unless explicitly stated otherwise, any mention of irradiance or solar irradiance refers specifically to Global Horizontal Irradiance.

Photovoltaic Power Output: PV power output refers to the electricity generated by solar panels from incoming solar radiation. While it is primarily driven by GHI [47], factors like temperature, and system losses also play a role. Under stable conditions, the relationship between GHI and PV output is roughly linear [31, 38]. Since PV output is a more actionable metric for grid management and energy planning, predicting it directly is often more desirable.

3.2 Nowcasting Architecture

We propose an architecture that encodes sky images into vector representations, which are augmented with auxiliary data and physics-based features. This representation captures information about the GHI, which is then effectively extracted by a regression model.

Let \mathcal{X} be the set of sky camera images, and \mathcal{D} be the dataset, defined as $\mathcal{D} = \{(X_i, \mathbf{A}_i, y_i)\}_{i=1}^N$, where $X_i \in \mathcal{X}$ represents the i -th sky image, $\mathbf{A}_i \in \mathbb{R}^k$ corresponds to the auxiliary features such as azimuth and zenith angles of the Sun, and $y_i \in \mathbb{R}^+$ are the corresponding solar irradiance measurements.

An encoder function $E : \mathcal{X} \rightarrow \mathbb{R}^d$ is defined that assigns a d -dimensional embedding vector to each image $X \in \mathcal{X}$:

$$\mathbf{Z} = E(X), \quad \mathbf{Z} \in \mathbb{R}^d$$

To leverage domain knowledge in solar power prediction, we introduce a set of additional features, \mathbf{P} , derived from the auxiliary measurements \mathbf{A} . These features incorporate established solar engineering principles, such as clear sky irradiance, and panel tilt and orientation, as defined in Subsection 3.4. The feature vector \mathbf{P} is given by:

$$\mathbf{P} \in \mathbb{R}^p$$

where p represents the number of physics-based features extracted from the auxiliary data.

The final feature representation $\mathbf{f} \in \mathbb{R}^{d+k+p}$ is constructed by concatenating the image embedding \mathbf{Z} , raw auxiliary measurements \mathbf{A} , and the physics-based features \mathbf{P} :

$$\mathbf{f} = \mathbf{Z} \oplus \mathbf{A} \oplus \mathbf{P}$$

where \oplus denotes the concatenation operation. This combined representation leverages data-driven features, visual features, and domain-specific engineering knowledge, providing a comprehensive characterization of each sample $(X_i, \mathbf{A}_i, y_i) \in \mathcal{D}$.

A regression function $R_\omega : \mathbb{R}^{d+k+p} \rightarrow \mathbb{R}^+$, parameterized by weights ω , is defined such that:

$$\hat{y} = R_\omega(\mathbf{f}) = R_\omega(E(X) \oplus \mathbf{A} \oplus \mathbf{P})$$

Nowcasting loss function $\mathcal{L}_{nowcast}(\omega)$ is defined as the average of the individual regression losses for each sample, where each individual loss measures the discrepancy between the predicted $\hat{y}_i = R_\omega(\mathbf{f}_i)$ and the true value y_i :

$$\mathcal{L}_{nowcast}(\omega) = \frac{1}{N} \sum_{i=1}^N \mathcal{L}(R_\omega(\mathbf{f}_i), y_i)$$

where $\mathcal{L}(R_\omega(\mathbf{f}_i), y_i)$ is the regression loss for the i -th sample. To learn the optimal parameters ω^* , we minimize $\mathcal{L}_{nowcast}(\omega)$ using gradient-based methods.

3.3 Forecasting Architecture

Our forecasting architecture processes sequences of sky images to predict GHI across multiple future intervals. Each image is encoded using the embedding and augmentation approach from Section 3.2. A time-series model captures a latent representation of past features, while predictable future covariates, such as the zenith angle, are precomputed and integrated as a vector. The combined past and future representations are then input into a regressor to generate GHI predictions.

A sequence of T images $X_{1:T} = \{X_1, X_2, \dots, X_T\}$ along with their corresponding auxiliary features $\mathbf{A}_{1:T} = \{\mathbf{A}_1, \mathbf{A}_2, \dots, \mathbf{A}_T\}$, where each $\mathbf{A}_t \in \mathbb{R}^k$ represents the auxiliary feature vector at time t , is given.

An encoder function E generates the vector representation $\mathbf{Z}_t = E(X_t) \in \mathbb{R}^d$ for each image at time step $t = 1, 2, \dots, T$. The physics-based features \mathbf{P}_t are derived from auxiliary measurements \mathbf{A}_t . The

final feature vectors $\mathbf{f}_t \in \mathbb{R}^{d+k+p}$ are obtained by concatenating the image embedding, auxiliary data, and physics-based features:

$$\mathbf{f}_t = \mathbf{Z}_t \oplus \mathbf{A}_t \oplus \mathbf{P}_t$$

where \oplus denotes concatenation, providing a comprehensive characterization of each sample $(X_t, \mathbf{A}_t, y_t) \in \mathcal{D}$.

Thus, the collection of feature vectors over the sequence of T time steps is given by:

$$\mathbf{F}_{1:T} = \{\mathbf{f}_1, \mathbf{f}_2, \dots, \mathbf{f}_T\}$$

where $\mathbf{F}_{1:T}$ represents the set of concatenated feature representations created for each timestamp in the sequence.

Given the collection of feature vectors $\mathbf{F}_{1:T} = \{\mathbf{f}_1, \mathbf{f}_2, \dots, \mathbf{f}_T\}$, a time-series model \mathcal{M} is used to encode the observed sequence into a latent vector $\mathbf{L} \in \mathbb{R}^m$, which captures the full context of the input data series while retaining its temporal patterns and dependencies:

$$\mathbf{L} = \mathcal{M}(\mathbf{F}_{1:T}) \in \mathbb{R}^m$$

where \mathcal{M} represents the time-series model that transforms the observed sequence of feature vectors $\mathbf{F}_{1:T}$ into a compact representation in the latent space \mathbb{R}^m .

To integrate known future information, derived from the spatiotemporal context of time and location, future covariate vectors $\mathbf{C}_{T+\tau_i} \in \mathbb{R}^q$ are constructed for each forecast time $T + \tau_i$. The full covariate vector $\mathbf{C} \in \mathbb{R}^{q \cdot H}$ is then formed by concatenating these individual representations across all forecast horizons:

$$\mathbf{C} = \bigoplus_{i=1}^H \mathbf{C}_{T+\tau_i}, \quad \mathbf{C}_{T+\tau_i} \in \mathbb{R}^q$$

We concatenate the future covariate vector \mathbf{C} with the latent representation of the past time steps \mathbf{L} , forming the final vector that encompasses all relevant information:

$$\mathbf{h} = \mathbf{L} \oplus \mathbf{C}$$

This ensures that both past contextual information as well as known future data contribute to the forecasting process.

Next, a regression function $R_\omega : \mathbb{R}^{m+q \cdot H} \rightarrow \mathbb{R}^H$, parameterized by ω , is applied to the vector $\mathbf{h} \in \mathbb{R}^{m+q \cdot H}$ to generate the corresponding predicted GHI values. The regressor outputs a vector $\hat{\mathbf{y}} \in \mathbb{R}^H$ of predicted GHI values for the forecast time intervals $T + \tau_1, T + \tau_2, \dots, T + \tau_H$:

$$\hat{\mathbf{y}} = R_\omega(\mathbf{h}) = [\hat{y}_{T+\tau_1}, \hat{y}_{T+\tau_2}, \dots, \hat{y}_{T+\tau_H}] \in \mathbb{R}^H$$

where each \hat{y}_i corresponds to the irradiance forecast for the time interval $T + \tau_i$, and the vector $\hat{\mathbf{y}}$ represents the full set of predicted irradiance values across all forecast intervals $T + \tau_1, T + \tau_2, \dots, T + \tau_H$.

Forecasting loss function $\mathcal{L}_{forecast}(\omega)$ is defined as the mean of the individual regression losses computed over all forecast intervals $T + \tau_j$ for each sample i . Specifically, the total loss is given by:

$$\mathcal{L}_{forecast}(\omega) = \frac{1}{N \cdot H} \sum_{i=1}^N \sum_{j=1}^H \mathcal{L}(\hat{y}_{T+\tau_j}^{(i)}, y_{T+\tau_j}^{(i)})$$

where $\mathcal{L}(\hat{y}_{T+\tau_j}^{(i)}, y_{T+\tau_j}^{(i)})$ is the individual regression loss for the forecast interval $T + \tau_j$ for sample i . To learn the optimal parameters

ω^* , we minimize $\mathcal{L}_{forecast}(\omega)$ using gradient-based optimization methods. The complete architecture is illustrated in Figure 1.

The Significance of Generalized Encoders: A key distinction of our approach is that in prior work [14, 16, 44], the encoder E is a vision model typically trained on data from a specific location and camera setup. Furthermore, studies aiming for generalizability typically rely on training models using a fusion of solar datasets from multiple locations [9, 33]. In contrast, we argue, and later demonstrate, that leveraging a foundation model, a highly generalizable feature extractor, provides a more robust E function. A foundation model not only matches the performance of site-specific encoders at a given location with a particular setup but also demonstrates an unparalleled advantage in generalizing across diverse locations and camera setups.

3.4 Physics-inspired Feature Engineering

Clear sky models [18, 30, 36, 45] are mathematical models that estimate the theoretical solar irradiance at a given location under cloud-free conditions, serving as a representation of the maximum possible radiation reaching the Earth’s surface. These models leverage fundamental atmospheric physics and employ mathematical formulations based on solar geometry [45], atmospheric transmittance [45], and radiative transfer [45] to derive estimations of GHI, DNI and DHI under clear sky conditions. The Ineichen clear sky model [18] requires inputs such as latitude, longitude, time, and date, which are readily available. This allows clear sky irradiance values to be readily computed and incorporated into our model as features, providing a reference for expected irradiance levels in the absence of cloud interference.

Physics behind solar irradiance: Solar irradiance, the power per unit area received from the Sun in the form of electromagnetic radiation, is measured in watts per square meter (W/m^2). The amount of solar irradiance received by a solar panel depends on additional site-specific factors, including the panel’s tilt and orientation angle, the Sun’s altitude and azimuth, and the geographic location’s latitude and longitude. We first look at the angle of incidence (θ) [25], i.e. the angle between the incoming solar rays and the normal to the surface of the solar panel. It can be calculated using the following formula:

$$\cos(\theta) = \cos(\theta_z) \cdot \cos(\beta) + \sin(\theta_z) \cdot \sin(\beta) \cdot \cos(\gamma - \alpha) \quad (2)$$

where θ_z and γ are the solar zenith and azimuth angles respectively. While β and α are the tilt and azimuth angles of the panel.

We calculate the effective irradiance by adding the three main components: direct, diffuse, and reflected irradiance (see below):

$$I_{panel} = DNI \cdot \cos(\theta) + DHI \cdot \frac{1 + \cos(\beta)}{2} + GHI \cdot \rho \cdot \frac{1 - \cos(\beta)}{2} \quad (3)$$

where I_{panel} is the effective irradiance and ρ is the ground reflectance.

4 SPIRIT IMPLEMENTATION

4.1 Nowcasting

In our approach, we utilize the pre-trained Google Vision Transformer (ViT) [11], a model with 632 million parameters, to generate

embeddings for sky camera images. To reduce sensor dependence and focus on image features, we exclude meteorological sensor data, incorporating only auxiliary variables such as zenith and azimuth angles, clear sky irradiance, panel tilt, and orientation. These image embeddings are subsequently concatenated with the auxiliary vector to form the final feature representation. The combined feature vectors, paired with their corresponding ground truth GHI values, are then used to train an XGBoost regressor within a supervised learning framework. The model is optimized by minimizing the Mean Squared Error (MSE) loss function, which measures the difference between the predicted and actual GHI values.

4.2 Forecasting

For forecasting, we employ the Google Vision Transformer (ViT) [11] to generate image embeddings, which are subsequently concatenated with the auxiliary variables to form a comprehensive feature representation. To account for temporal dependencies, we input a sequence of six images, representing a 1-hour context window, into a transformer-based time-series encoder [46]. This encoder processes the temporal sequence and learns a latent representation of the past context, which is then fused with a future covariate vector that includes azimuth and zenith angles, as well as clear sky GHI. The resulting representation is passed through a multi-layer perceptron (MLP) to predict the solar irradiance for the 1-hour, 2-hour, 3-hour, and 4-hour forecast intervals. This implementation exemplifies one approach in our framework, with additional variations incorporating different vision encoders of varied sizes in the ablation studies detailed in Section 7.

5 EVALUATION METHODOLOGY

5.1 Datasets

We evaluate our methods using three publicly available datasets: TSI880 [5], ASI16 [5], and SKIPP’D [32]. The TSI880 and ASI16 datasets, both collected from the NREL Solar Radiation Research Laboratory in Golden, Colorado, provide sky images captured every 10 minutes along with corresponding GHI values and auxiliary data such as air temperature and relative humidity and only differ in camera setup and sensors, with the ASI16 dataset capturing higher-resolution images. The SKIPP’D dataset, collected from Stanford University, consists of raw sky images captured every minute and PV power output data, prioritizing finer temporal granularity at the expense of image quality. For more details, refer to Appendix A.

We utilize the TSI880 and ASI16 datasets to investigate the impact of camera setup at the same location. To explore location and task shifts, we use the SKIPP’D dataset to evaluate the performance of models trained on GHI data in predicting PV power output. The SKIPP’D dataset features lower-resolution images and lacks meteorological data, thereby presenting a more challenging task by limiting the contextual information typically leveraged by prior models [14, 44]. To ensure the models learn from higher-quality, information-rich datasets, we train exclusively on the TSI and ASI datasets while evaluation is done across all the datasets, including the more challenging SKIPP’D, allowing us to assess how well the models generalize to lower-quality data and increased domain shifts.

Table 1: Nowcasting performance across multiple datasets: SPIRIT and Gao et al.’s [14] model trained on one dataset for a year are evaluated with nMAP both in a zero-shot setting and on the same dataset, with testing on TSI 2021, ASI 2021, and SKIPP’D 2017. We observe comparable performance when tested in the training setup, but our model demonstrates significantly better zero-shot performance in a new location.

Trained on	Tested on	SPIRIT	Gao et al. [14]
TSI	ASI	27.17 (-62.49)	89.66
	SKIPP’D	35.94 (-60.94)	96.43
<hr/>			
ASI	TSI	9.04 (+0.08)	8.96
	TSI	28.86 (-46.65)	75.51
	SKIPP’D	32.98 (-57.69)	90.67
<hr/>			
	ASI	9.08 (+0.95)	8.13

5.2 Performance Metrics

We assess the effectiveness of the predicted values using the normalized Mean Absolute Percentage error (nMAP), defined as:

$$\text{nMAP} = \frac{1}{N} \sum_{i=1}^N \frac{|y_i - \hat{y}_i|}{\frac{1}{N} \sum_{i=1}^N y_i} \times 100 \quad (4)$$

where y_i represents the actual value and \hat{y}_i represents the predicted value for the i -th sample, with $i \in \{1, \dots, N\}$. It is commonly used for solar irradiance prediction as the normalization ensures that models can be assessed uniformly on datasets with varied value ranges, avoiding biased assessments due to scale differences.

5.3 Baselines

To benchmark our proposed method, we compare its performance against the state-of-the-art baseline, Gao *et al.* [14], who demonstrate state-of-the-art performance for nowcasting and forecasting by training a vision transformer [11] from the ground up using 10 years of site-specific data [5, 14, 44]. Their approach for forecasting utilizes a temporal transformer [46], also trained on the same duration of data. To ensure a fair comparison, we reproduced their architecture and conducted experiments under the same conditions for both Gao *et al.*’s [14] model and SPIRIT.

5.4 Zero-shot Transfer Learning

To evaluate the zero-shot generalization performance of our models, we analyze two distinct transfer learning scenarios. The first scenario examines intra-location generalization, where the models are trained and tested in the same geographic location but under varying camera setups. While the environmental conditions remain consistent, variations in camera setup, viewing angles, and image resolutions exist between the training and testing phases. When image-based models are trained on data from a particular camera setup, they learn to associate specific regions of the image with key features—such as the position of the sun, cloud formations, or atmospheric conditions—that influence the predicted output. However, when the camera setup is altered, the spatial mapping of these features within the image shifts. To assess how well the models

Table 2: Forecasting performance across multiple datasets and forecast intervals: SPIRIT and Gao et al.’s [14] model trained on one dataset are evaluated with nMAP error both in a zero-shot setting and on the same dataset, with testing on TSI 2021, ASI 2021, and SKIPP’D 2017 across four forecast intervals: 1hr, 2hr, 3hr, and 4hr.

Interval	Trained on	Tested on	SPIRIT	Gao et al. [14]
1hr	TSI	ASI	29.99 (-5.75)	35.74
		SKIPP’D	32.93 (-5.95)	38.88
	ASI	TSI	18.96 (-1.00)	19.96
		TSI	26.85 (-2.19)	29.04
		SKIPP’D	27.33 (-14.35)	41.68
		ASI	19.23 (+0.02)	19.21
<hr/>				
2hr	TSI	ASI	31.71 (-5.89)	37.60
		SKIPP’D	29.01 (-14.80)	43.81
	ASI	TSI	21.77 (-0.87)	22.64
		TSI	28.64 (-1.01)	30.65
		SKIPP’D	26.29 (-21.63)	47.92
		ASI	21.51 (-0.47)	21.98
<hr/>				
3hr	TSI	ASI	34.41 (-3.36)	37.77
		SKIPP’D	30.26 (-17.10)	47.36
	ASI	TSI	25.46 (-0.84)	26.30
		TSI	31.65 (-1.5)	33.15
		SKIPP’D	30.26 (-22.89)	53.15
		ASI	24.78 (-0.89)	25.67
<hr/>				
4hr	TSI	ASI	38.00 (-1.58)	39.58
		SKIPP’D	34.63 (-17.15)	51.78
	ASI	TSI	29.89 (-1.69)	31.58
		TSI	35.86 (-0.99)	36.85
		SKIPP’D	36.97 (-13.20)	50.17
		ASI	29.29 (-1.73)	31.02

handle such variations, we train them using the TSI dataset and evaluate them on the ASI dataset, and vice versa.

The second scenario focuses on cross-location and cross-task generalization, where models trained in one geographic location are tested in another with different environmental and sensor characteristics. We train on the TSI and ASI datasets and evaluate on the SKIPP’D dataset, with the task shifting from predicting GHI to PV power output. Since GHI and PV output have a nearly linear correlation [47], this serves as a valid example of heterogeneous transfer learning. To account for the significant scale difference between GHI and PV output, model outputs are normalized for comparability. We conduct experiments for both nowcasting and forecasting tasks, training the models for one year and testing them on another year to account for seasonal variations, thus ensuring a fair evaluation. The nMAP errors are reported in Table 1 for nowcasting and Table 2 for forecasting, comparing SPIRIT with the state-of-the-art in both the zero-shot transfer learning setups and

the traditional settings, where the models are trained and tested using data from the same location and setup, but different years.

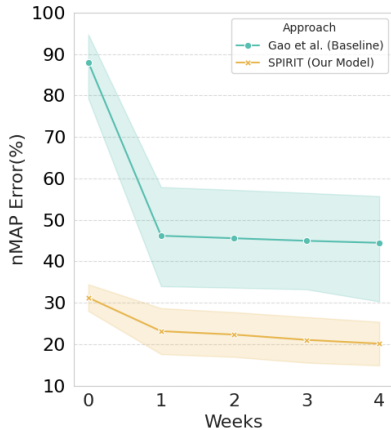


Figure 2: We compare the nowcasting performance of SPIRIT and Gao *et al.* using nMAP error. The solid lines represent the average performance across different fine-tuning training sizes, measured in weeks of data. The shaded regions indicate the $x\%$ confidence interval, reflecting variability across multiple experimental settings, including training on one dataset and testing on another, as well as selecting fine-tuning data from different starting points throughout the year.

5.5 Fine-tuning with Limited Data

Building upon our zero-shot transfer learning experiments, we now investigate the adaptability of our models in a fine-tuning framework, where a limited amount of labeled data from the target domain is available for fine-tuning. This scenario closely resembles practical deployment conditions, where prolonged data collection is often infeasible, and models must quickly adapt to new locations with minimal supervision. We evaluate transfer learning with limited data in two scenarios: intra-location adaptation and cross-location adaptation, as in Subsection 5.4.

For both experimental setups, we perform fine-tuning using progressively increasing amounts of labeled data from the target domain—specifically, one, two, three, and four weeks of data from a full year for nowcasting, and two, four, eight, twelve, and sixteen weeks of data for forecasting with testing done on the remaining data from the year. Given the greater complexity of forecasting, we extend the fine-tuning experiment to a larger time frame. Additionally, due to the requirement for temporal consistency in the time series data, as discussed in Subsection A.2, the number of nowcasting samples for a given time period exceeds that of forecasting samples. We implement a selective fine-tuning approach, where only the regressors (see Figure 1) are updated, while the rest of the model is frozen. This ensures that the pre-trained feature representations, which capture generalizable spatiotemporal patterns, remain intact while allowing the model to adapt to location- and camera-specific variations. As demonstrated in prior work [33, 42, 50], fine-tuning only the final layers achieves competitive adaptation performance

while mitigating the risk of overfitting to the limited target data. The nowcasting metrics are shown in Figure 2, and the forecasting metrics are depicted in Figure 3.

6 RESULTS

6.1 Zero-shot Transfer Learning

Tables 1 and 2 present the results for zero-shot transfer learning, demonstrating that our model consistently outperforms the state-of-the-art baseline across both cross-location and cross-setup scenarios in both nowcasting and forecasting tasks. When transitioning between camera setups within the same location, our model consistently shows better performance relative to the baseline. However, more notably, when moving across different locations, our model achieves up to 45% improvement. In this more complex cross-location setting, our model significantly outperforms the baseline, highlighting its superior generalizability and robustness. Furthermore, even in the traditional setup where models are trained and tested on the same location, our approach demonstrates enhanced forecasting performance, further emphasizing its effectiveness across diverse deployment conditions.

6.2 Fine-tuning with Limited Data

For the analysis of fine-tuning results, we merge cross-setup and cross-location scenarios to ensure a sufficient number of data points for robust confidence interval plots, as depicted in both the nowcasting (Figure 2) and forecasting (Figure 3) tasks. Since nowcasting is a relatively simpler task, both models exhibit rapid improvement within the first week. However, the baseline model reaches performance saturation early, at approximately 45%, while our model continues to reduce its error, achieving a significant improvement, dropping below 20% within four weeks.

In forecasting, SPIRIT consistently outperforms the baseline, demonstrating notably lower variance, particularly in data-limited settings (0-2 weeks of data). This underscores SPIRIT’s superior stability and reliability, with its nMAP error remaining consistently below that of the baseline. In contrast, the baseline model exhibits higher variance, indicating greater inconsistency and confusion in its performance when limited data is available. Both models experience a typical performance decline as the forecasting horizon extends from 1-hour to 4-hour forecasts, driven by the increased uncertainty over longer time horizons. Nonetheless, SPIRIT’s consistently lower variance and sustained performance highlight its robustness and its ability to adapt more effectively to challenging conditions. The transition from a zero-shot configuration to fine-tuning results in noticeable performance improvements; however, the gains diminish after approximately eight weeks of fine-tuning, suggesting that extended fine-tuning beyond this period yields only marginal additional benefits. All the results are in Appendix C.

7 ABLATION STUDIES

7.1 Investigating Different Vision Encoders

We examine the impact of different vision models on SPIRIT’s performance, also highlighting the versatility of our system across different foundation models. We evaluate the CNN-based ResNet-152 [17], the vision transformer-based DINOv2 Giant [35], and our

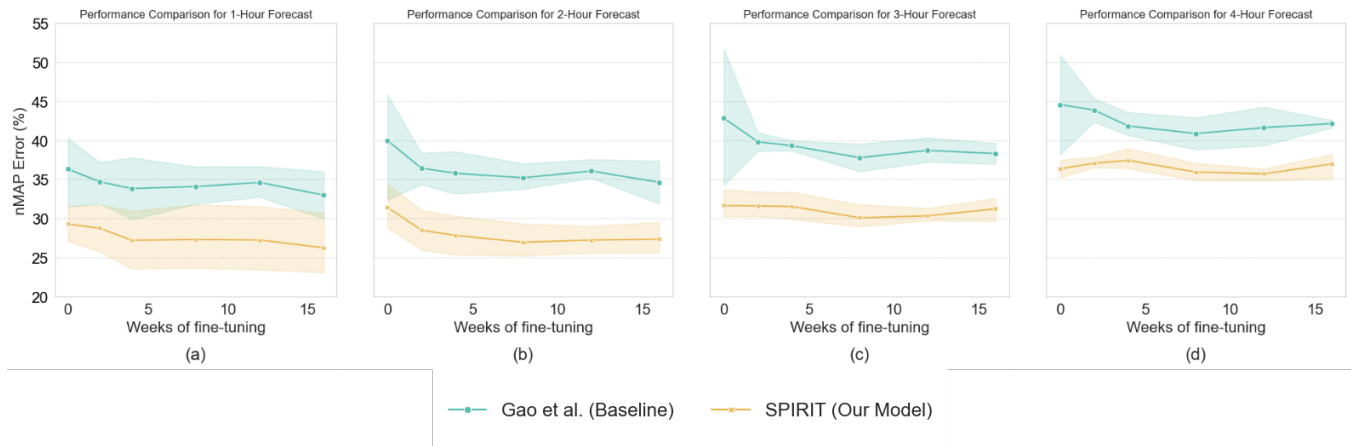


Figure 3: We compare the forecasting performance of SPIRIT and Gao *et al.* using nMAP error across different forecast intervals. Subfigures (a), (b), (c), and (d) correspond to 1-hour, 2-hour, 3-hour, and 4-hour forecasting, respectively. The solid lines represent the average performance for each forecast interval, with varying fine-tuning training sizes measured in weeks of data. The shaded regions denote the 95% confidence interval, illustrating the variability across multiple experimental settings, including training on one dataset and testing on another, as well as selecting weeks of contiguous fine-tuning data from different starting points throughout the year. SPIRIT exhibits consistently low variance compared to the baseline, particularly in settings with severely limited data, demonstrating its ability to maintain stability. In contrast, the baseline shows high variance, indicating uncertainty in its predictions.

implementation using Google ViT-Huge [11]. Results summarized in Table 3, demonstrate that the ViT-based models consistently outperform the ResNet-152 CNN model, which can be attributed to the superior capability of ViT architectures in capturing global image features [22].

Table 3: We explore the impact of using different vision encoders on the overall model performance for nowcasting and forecasting, with training on TSI 2020 and testing on TSI 2021, measured by nMAP error.

Model	Nowcast	Forecast			
		+1hr	+2hr	+3hr	+4hr
ResNet-152	10.50	24.56	27.82	31.23	35.85
DINOv2 Giant	9.74	21.22	23.56	27.93	33.13
Google ViT-Huge	9.32	19.96	22.64	26.30	31.58

7.2 Foundation Model Size

Table 4 presents an analysis of how the size of the foundation model influences the performance of our nowcasting and forecasting architectures. Although increasing model size has traditionally been linked to performance gains, we observe that beyond a certain threshold, further scaling yields diminishing returns. This suggests that larger models do not always lead to better performance. In fact, models with 304M and 86M parameters outperform their larger counterparts with 632M parameters in forecasting and nowcasting, respectively. This aligns with recent work, which highlights that adjusting model size based on a computational budget, rather than

blindly increasing model size, can lead to more efficient architectures with reduced inference costs [4].

Table 4: We evaluate the impact of varying size of the Google ViT vision encoder on the overall performance of the model for both nowcasting and forecasting tasks, with training on TSI 2020 and testing performed on TSI 2021.

Model Parameters	Nowcast	Forecast			
		+1hr	+2hr	+3hr	+4hr
86M	9.14	21.92	24.07	28.73	34.50
304M	9.45	19.58	21.95	25.54	30.60
632M	9.32	19.96	22.64	26.30	31.58

8 CONCLUSION

This work addresses a critical challenge in solar irradiance forecasting: adapting models to new geographic locations with no prior data. By utilizing transfer learning and pre-trained models, SPIRIT generalizes well to new locations, reducing the reliance on large, location-specific datasets. As more site-specific data becomes available post-deployment, the system can be effectively fine-tuned, improving prediction accuracy and supporting better energy yield estimates and operational planning. Additionally, SPIRIT’s modular design allows for the seamless integration of any emerging vision models, ensuring that the framework remains up-to-date with the latest advancements. This scalable solution for solar irradiance forecasting can accelerate the deployment of solar farms—particularly in remote and emerging markets. SPIRIT supports the transition to

renewable energy by enhancing the reliability, cost-effectiveness, and accessibility of solar energy generation.

9 FUTURE WORK AND LIMITATIONS

One key limitation is that the datasets used for evaluation are all from North America, largely due to the limited availability of publicly accessible datasets from other regions. Specifically, the solar movement patterns and dynamics change in the Southern Hemisphere and need to be studied. To improve the generalizability of our system, future work will incorporate data from other continents. Additionally, while our model performs well, the use of foundation models introduces real-time inference costs and computational overheads. Future efforts will focus on reducing computational efficiency, enabling deployment on resource-constrained edge devices without sacrificing accuracy.

REFERENCES

- [1] 2023. World Solar Market Report 2023.
- [2] Mahmoud Y. Abido, Zahir Mahmud, Pedro Andrés Sánchez-Pérez, and Sarah R. Kurtz. 2022. Seasonal challenges for a California renewable- energy-driven grid. *iScience* 25, 1 (2022), 103577. <https://doi.org/10.1016/j.isci.2021.103577>
- [3] Anup Agarwal, Jinghan Sun, Shadi Noghabi, Srinivasan Iyengar, Anirudh Badam, Ranveer Chandra, Srinivasan Seshan, and Shivkumar Kalyanaraman. 2021. Re-designing data centers for renewable energy. In *Proceedings of the 20th ACM Workshop on Hot Topics in Networks*. 45–52.
- [4] Ibrahim Alabdulmohsin, Xiaohua Zhai, Alexander Kolesnikov, and Lucas Beyer. 2023. Getting ViT in Shape: Scaling Laws for Compute-Optimal Model Design. In *Thirty-seventh Conference on Neural Information Processing Systems*. <https://openreview.net/forum?id=en4LGxp9E>
- [5] A. Andreas and T. Stoffel. 1981. NREL Solar Radiation Research Laboratory (SRRL): Baseline Measurement System (BMS); Golden, Colorado (Data). <https://doi.org/10.5439/1052221> NREL Report No. DA-5500-56488.
- [6] Hichem Idris Aouidad and Abdelhamid Bouhelal. 2024. Machine learning-based short-term solar power forecasting: a comparison between regression and classification approaches using extensive Australian dataset. *Sustainable Energy Research* 11, 1 (2024), 28.
- [7] Noman Bashir, Tian Guo, Mohamad Hajiesmaili, David Irwin, Prashant Shenoy, Ramesh Sitaraman, Abel Souza, and Adam Wierman. 2021. Enabling sustainable clouds: The case for virtualizing the energy system. In *Proceedings of the ACM Symposium on Cloud Computing*. 350–358.
- [8] Abdelkader Dairi, Fouzi Harrou, Ying Sun, and Sofiane Khadraoui. 2020. Short-term forecasting of photovoltaic solar power production using variational auto-encoder driven deep learning approach. *Applied Sciences* 10, 23 (2020), 8400.
- [9] Milan Despotovic, Cyril Voyant, Luis Garcia-Gutierrez, Javier Almorox, and Gilles Notton. 2024. Solar irradiance time series forecasting using auto-regressive and extreme learning methods: Influence of transfer learning and clustering. *Applied Energy* 365 (2024), 123215. <https://doi.org/10.1016/j.apenergy.2024.123215>
- [10] Soumyabrata Dev, Florian M Savoy, Yee Hui Lee, and Stefan Winkler. 2019. Estimating solar irradiance using sky imagers. *Atmospheric Measurement Techniques* 12, 10 (2019), 5417–5429.
- [11] Alexey Dosovitskiy. 2020. An image is worth 16x16 words: Transformers for image recognition at scale. *arXiv preprint arXiv:2010.11929* (2020).
- [12] M Erdmann, E Geiser, Y Rath, and M Rieger. 2020. Physics inspired feature engineering with Lorentz Boost Networks. In *Journal of Physics: Conference Series*, Vol. 1525. IOP Publishing, 012107.
- [13] Tolulope Olumuyiwa Falope, Liyun Lao, and Dawid Hanak. 2024. A three-step weather data approach in solar energy prediction using machine learning. *Renewable Energy Focus* 50 (2024), 100615.
- [14] Huiyu Gao and Miaomiao Liu. 2022. Short-term Solar Irradiance Prediction from Sky Images with a Clear Sky Model. In *2022 IEEE/CVF Winter Conference on Applications of Computer Vision (WACV)*. 3074–3082. <https://doi.org/10.1109/WACV51458.2022.00313>
- [15] Joshua Edward Hammond, Ricardo A. Lara Orozco, Michael Baldea, and Brian A. Korgel. 2024. Short-Term Solar Irradiance Forecasting Under Data Transmission Constraints. *arXiv:2403.12873*
- [16] Ali Hasan. 2023. Predicting Solar Irradiance at Several Time Horizons Using Machine Learning Algorithms. (06 2023).
- [17] Kaiming He, Xiangyu Zhang, Shaoqing Ren, and Jian Sun. 2016. Deep residual learning for image recognition. In *Proceedings of the IEEE conference on computer vision and pattern recognition*. 770–778.
- [18] Pierre Ineichen and Richard Perez. 2002. A new air mass independent formulation for the Linke turbidity coefficient. *Solar Energy* 73 (09 2002), 151–157. [https://doi.org/10.1016/S0038-092X\(02\)00045-2](https://doi.org/10.1016/S0038-092X(02)00045-2)
- [19] Srinivasan Iyengar, Stephen Lee, David Irwin, and Prashant Shenoy. 2016. Analyzing energy usage on a city-scale using utility smart meters. In *Proceedings of the 3rd ACM International Conference on Systems for Energy-Efficient Built Environments*. 51–60.
- [20] Srinivasan Iyengar, Navin Sharma, David Irwin, Prashant Shenoy, and Krithi Ramamritham. 2014. SolarCast: a cloud-based black box solar predictor for smart homes. In *Proceedings of the 1st ACM Conference on Embedded Systems for Energy-Efficient Buildings*. 40–49.
- [21] Srinivasan Iyengar, Navin Sharma, David Irwin, Prashant Shenoy, and Krithi Ramamritham. 2017. A cloud-based black-box solar predictor for smart homes. *ACM Transactions on Cyber-Physical Systems* 1, 4 (2017), 1–24.
- [22] Kishaan Jeeveswaran, Senthilkumar Kathiresan, Arnab Varma, Omar Magdy, Bahram Zonooz, and Elahe Arani. 2022. A Comprehensive Study of Vision Transformers on Dense Prediction Tasks. *arXiv:2201.08683 [cs.CV]* <https://arxiv.org/abs/2201.08683>
- [23] Paul L Joskow. 2012. Creating a smarter US electricity grid. *Journal of Economic Perspectives* 26, 1 (2012), 29–48.
- [24] Vladimir Kostylev, Alexandre Pavlovski, et al. 2011. Solar power forecasting performance—towards industry standards. In *1st international workshop on the integration of solar power into power systems, Aarhus, Denmark*. Energynautics GmbH Mühlstraße Langen, Germany, 1–8.
- [25] Sandia National Laboratories. [n. d.]. PV Performance Modeling Collaborative (PVP/MC). <https://pvpmc.sandia.gov/modeling-guide/1-weather-design-inputs/plane-of-array-poa-irradiance/calculating-poa-irradiance/angle-of-incidence/>. Accessed: 2025-01-15.
- [26] Jared A. Lee, Sue Ellen Haupt, Pedro A. Jiménez, Matthew A. Rogers, Steven D. Miller, and Tyler C. McCandless. 2017. Solar Irradiance Nowcasting Case Studies near Sacramento. *Journal of Applied Meteorology and Climatology* 56, 1 (2017), 85–108. <https://doi.org/10.1175/JAMC-D-16-0183.1>
- [27] Stephen Lee, Srinivasan Iyengar, David Irwin, and Prashant Shenoy. 2016. Shared solar-powered EV charging stations: Feasibility and benefits. In *2016 Seventh International Green and Sustainable Computing Conference (IGSC)*. IEEE, 1–8.
- [28] Francis M. Lopes, Ricardo Conceição, Hugo G. Silva, Rui Salgado, and Manuel Collares-Pereira. 2021. Improved ECMWF forecasts of direct normal irradiance: A tool for better operational strategies in concentrating solar power plants. *Renewable Energy* 163 (2021), 755–771. <https://doi.org/10.1016/j.renene.2020.08.140>
- [29] Dávid Markovics and Martin János Mayer. 2022. Comparison of machine learning methods for photovoltaic power forecasting based on numerical weather prediction. *Renewable and Sustainable Energy Reviews* 161 (2022), 112364.
- [30] R.W. Mueller, K.F. Dagestad, P. Ineichen, M. Schroedter-Homscheidt, S. Cros, D. Dumortier, R. Kuhlmann, J.A. Olseth, G. Piernavieja, C. Reise, L. Wald, and D. Heinemann. 2004. Rethinking satellite-based solar irradiance modelling: The SOLIS clear-sky module. *Remote Sensing of Environment* 91, 2 (2004), 160–174. <https://doi.org/10.1016/j.rse.2004.02.009>
- [31] Ali Nather Tuaimah and Shaker Al-Saidi. 2019. Investigation the effect of the temperature and irradiance on the output parameters of solar cell. *University of Thi-Qar Journal of Science* 7 (06 2019). <https://doi.org/10.32792/utq/utjs/v7i1.265>
- [32] Yuhao Nie, Xiatong Li, Andea Scott, Yuchi Sun, Vignesh Venugopal, and Adam Brandt. 2023. SKIPP'D: A SKY Images and Photovoltaic Power Generation Dataset for short-term solar forecasting. *Solar Energy* 255 (2023), 171–179. <https://doi.org/10.1016/j.solener.2023.03.043>
- [33] Yuhao Nie, Quentin Paletta, Andea Scott, Luis Martin Pomares, Guillaume Arbod, Sgouris Sgouridis, Joan Lasenby, and Adam Brandt. 2024. Sky image-based solar forecasting using deep learning with heterogeneous multi-location data: Dataset fusion versus transfer learning. *Applied Energy* 369 (2024), 123467. <https://doi.org/10.1016/j.apenergy.2024.123467>
- [34] Agusman Partogi Ompusunggu and Erik Hostens. 2021. Physics-Inspired Feature Engineering for Condition Monitoring of Alternating Current-Powered Solenoid-Operated Valves. In *International Conference on Maintenance, Condition Monitoring and Diagnostics*. Springer, 139–151.
- [35] Maxime Oquab, Timothée Darcet, Théo Moutakanni, Huy Vo, Marc Szafraniec, Vasil Khalidov, Pierre Fernandez, Daniel Haziza, Francisco Massa, Alaaeldin El-Nouby, et al. 2023. Dinov2: Learning robust visual features without supervision. *arXiv preprint arXiv:2304.07193* (2023).
- [36] Richard Perez, Pierre Ineichen, Kathy Moore, Marek Kmiecik, Cyril Chain, Ray George, and Frank Vignola. 2002. A new operational model for satellite-derived irradiances: description and validation. *Solar Energy* 73, 5 (2002), 307–317. [https://doi.org/10.1016/S0038-092X\(02\)00122-6](https://doi.org/10.1016/S0038-092X(02)00122-6)
- [37] Rial A Rajagukguk, Raihan Kamil, and Hyun-Jin Lee. 2021. A deep learning model to forecast solar irradiance using a sky camera. *Applied Sciences* 11, 11 (2021), 5049.
- [38] Amelia Razak, Y.M Irwan, W.Z. Leow, M Irwanto, I. Safwati, and M. Zhafarina. 2016. Investigation of the Effect Temperature on Photovoltaic (PV) Panel Output

- Performance. *International Journal on Advanced Science, Engineering and Information Technology* 6, 5 (Oct. 2016), 682–688. <https://doi.org/10.18517/ijaseit.6.5.938>
- [39] Jan Remund and Stefan Müller. 2012. SOLAR FORECAST SURVEY RESULTS. <https://doi.org/10.13140/2.1.3826.3681>
- [40] Jhuma Sadhukhan. 2022. Net zero electricity systems in global economies by life cycle assessment (LCA) considering ecosystem, health, monetization, and soil CO2 sequestration impacts. *Renewable Energy* 184 (2022), 960–974.
- [41] Rahul Saraswat, Deepak Jhanwar, and Manish Gupta. 2023. Sky Image Classification Based Solar Power Prediction Using CNN. *Traitement du Signal* 40, 4 (2023).
- [42] Elissaios Sarmas, Nikos Dimitropoulos, Vangelis Marinakis, Zoi Mylona, and H. Doukas. 2022. Transfer learning strategies for solar power forecasting under data scarcity. *Scientific Reports* 12 (08 2022). <https://doi.org/10.1038/s41598-022-18516-x>
- [43] Zekai Sen. 2008. *Solar energy fundamentals and modeling techniques: atmosphere, environment, climate change and renewable energy*. Springer Science & Business Media.
- [44] Talha Ahmad Siddiqui, Samarth Bharadwaj, and Shivkumar Kalyanaraman. 2019. A Deep Learning Approach to Solar-Irradiance Forecasting in Sky-Videos. *2019 IEEE Winter Conference on Applications of Computer Vision (WACV)* (2019), 2166–2174. <https://api.semanticscholar.org/CorpusID:58006621>
- [45] Joshua S Stein, Clifford W Hansen, and Matthew J Reno. 2012. *Global horizontal irradiance clear sky models: implementation and analysis*. Technical Report. Sandia National Laboratories (SNL), Albuquerque, NM, and Livermore, CA (United States). <https://doi.org/10.2172/1039404>
- [46] A Vaswani. 2017. Attention is all you need. *Advances in Neural Information Processing Systems* (2017).
- [47] Alba Vilanova, Bo-Young Kim, Chang Kim, and Hyun-Goo Kim. 2020. Linear-Gompertz Model-Based Regression of Photovoltaic Power Generation by Satellite Imagery-Based Solar Irradiance. *Energies* 13 (02 2020), 781. <https://doi.org/10.3390/en13040781>
- [48] Jin Xu, Shinjae Yoo, Dantong Yu, Dong Huang, John Heiser, and Paul Kalb. 2015. Solar irradiance forecasting using multi-layer cloud tracking and numerical weather prediction. In *Proceedings of the 30th Annual ACM Symposium on Applied Computing (Salamanca, Spain) (SAC '15)*. Association for Computing Machinery, New York, NY, USA, 2225–2230. <https://doi.org/10.1145/2695664.2695812>
- [49] Jiajia Yang, Zhao Yang Dong, Fushuan Wen, Qixin Chen, Fengji Luo, Weijia Liu, and Junpeng Zhan. 2020. A penalty scheme for mitigating uninstructed deviation of generation outputs from variable renewables in a distribution market. *IEEE Transactions on Smart Grid* 11, 5 (2020), 4056–4069.
- [50] Siyu Zhou, Lin Zhou, Mingxuan Mao, and Xinze Xi. 2020. Transfer Learning for Photovoltaic Power Forecasting with Long Short-Term Memory Neural Network. In *2020 IEEE International Conference on Big Data and Smart Computing (BigComp)*. 125–132. <https://doi.org/10.1109/BigComp48618.2020.00-87>
- [51] Orr Zohar, Alejandro Lozano, Shelly Goel, Serena Yeung, and Kuan-Chieh Wang. 2023. Open World Object Detection in the Era of Foundation Models. *arXiv preprint arXiv:2312.05745* (2023).

A DATASET DETAILS

A.1 Overview of Datasets

TSI880 Dataset: The TSI880 dataset is collected from the NREL Solar Radiation Research Laboratory in Golden, Colorado. The camera captures an image every 10 minutes from 7:50 to 16:40 daily, providing raw sky images along with corresponding global horizontal irradiance values. Additionally, the dataset includes auxiliary information such as air temperature, relative humidity, azimuth angle, and zenith angle.

ASI16 Dataset: The ASI16 dataset is also sourced from the Solar Radiation Research Laboratory in Golden, Colorado, but it differs in that the camera setup captures images at a higher resolution. Similar to the TSI880 dataset, it provides global horizontal irradiance values and auxiliary data including azimuth angle, zenith angle, air temperature, relative humidity, and average wind speed.

SKIPP'D Dataset: The SKIPP'D dataset consists of raw sky images and photovoltaic (PV) power output data collected from Stanford University, California, USA. Images are captured every minute with a resolution of 64×64 pixels, emphasizing finer temporal granularity at the expense of lower image resolution.

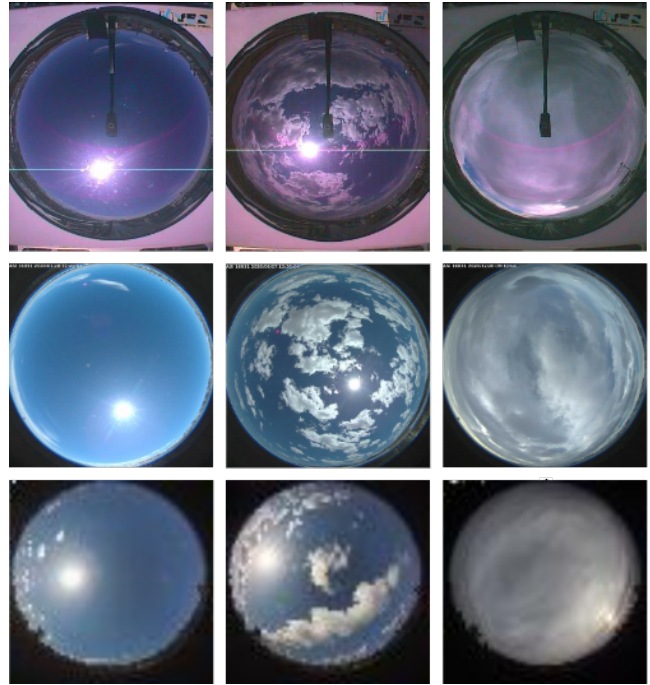


Figure 4: Examples of sunny, partly cloudy, and overcast conditions, captured by different sky cameras, are shown from left to right, across the three datasets: TSI, ASI, and SKIPP'D, displayed from top to bottom.

A.2 Temporal Consistency in Forecasting

Valid samples for forecasting are formed such that all the data points from time steps 1 to T , and their corresponding forecast intervals $T + \tau_1, T + \tau_2, \dots, T + \tau_H$, fall within the same day. This is an essential requirement because the predictions for future intervals rely on the assumption that both historical and forecast data belong to the same day. Using data from the current day to predict values for the following day is not a valid forecasting approach, as the discontinuity between days renders such predictions unreliable. Any samples that violate this condition are considered invalid and are excluded from training or evaluation.

B CLEAR SKY GLOBAL HORIZONTAL IRRADIANCE

Clear Sky Global Horizontal Irradiance (GHI) is the solar irradiance received on a horizontal surface under cloud-free conditions. Most of the time, it serves as an upper bound for the actual GHI at a given location and time.

Clear Sky GHI plays a key role in solar forecasting by serving as a baseline for estimating how much clouds reduce solar irradiance. By comparing actual irradiance with Clear Sky GHI, we can get an estimate of the impact of cloud cover, which helps in enhancing short-term predictions, and improving the accuracy of forecasting models.

Given the latitude and longitude of a location, the clear sky values can be estimated for any timestamp. This becomes very

Table 5: A Comparative Overview of the TSI880, ASI16, and SKIPP'D Datasets: Key Attributes Including Geographical Location, Data Provided, Image Resolution, Collection Frequency, and Annual Sample Size

Attribute	TSI880 Dataset	ASI16 Dataset	SKIPP'D Dataset
Location	Golden, Colorado, USA	Golden, Colorado, USA	Stanford, California, USA
Data Type	Sky images & Irradiance data	Sky images & Irradiance data	Sky images & PV power output
Data Frequency	10-minutes	10-minutes	1-minute
Image Resolution	288x352	1536x1536	64x64
Camera Model	Aero-Laser TSI-880	EKO ASI-16	Hikvision DS-2CD6362F-IV
Number of Samples / Year	24,948	25,107	121,125

useful in solar forecasting, as this value would give a reference of how much the prediction needs to be.

Clear Sky GHI is computed using mathematical models incorporating solar position, atmospheric transmittance, and radiative transfer principles. A common approach is the Ineichen-Perez model [45]:

$$GHI_{\text{clear}} = I_0 \cdot \tau \cdot \cos(\theta_z) \quad (5)$$

where I_0 is the extraterrestrial irradiance (W/m^2), τ is the atmospheric transmittance factor, θ_z is the solar zenith angle.

B.1 Extraterrestrial Irradiance (I_0)

Extraterrestrial irradiance (I_0) is the solar irradiance just outside Earth's atmosphere, slightly varying due to Earth's elliptical orbit around the Sun. It is given by:

$$I_0 = S_c \cdot \left(1 + 0.033 \cos\left(\frac{2\pi n}{365}\right) \right) \quad (6)$$

where $S_c = 1367 \text{ W}/\text{m}^2$ (solar constant), n is the day of the year (1 for January 1, 365 for December 31).

B.2 Atmospheric Transmittance (τ)

The atmospheric transmittance τ accounts for the attenuation of solar radiation by the atmosphere. It is often estimated using empirical models, such as the Ineichen-Perez model [45]:

$$\tau = a \cdot e^{-b \cdot m} \quad (7)$$

where a, b are empirical coefficients dependent on location and aerosol content, m is the air mass, given by [18]:

$$m = \frac{1}{\cos(\theta_z) + 0.15(93.885 - \theta_z)^{-1.253}} \quad (8)$$

where θ_z is the solar zenith angle.

C FINE-TUNING DETAILED RESULTS

C.1 Nowcasting

To understand the impact of fine-tuning duration and the training size, we conducted a series of experiments by varying the amount of training data used for fine-tuning, by using subsets of the data consisting of 1, 2, 3, and 4 weeks.

Our results show that even with only one week of training data at a new location, the fine-tuned model performs remarkably well.

Furthermore, in all experimental configurations, our model significantly outperforms the baseline.

Detailed results for these experiments are presented in Tables 6-9.

Table 6: Nowcasting Performance with 1 week training

Trained on	Finetuned on	SPIRIT	Gao et al. [14]
TSI	ASI	20.23	52.01
	SKIPP'D	29.89	63.82
ASI	TSI	14.99	27.98
	SKIPP'D	27.51	40.92

Table 7: Nowcasting Performance with 2 weeks training

Trained on	Finetuned on	SPIRIT	Gao et al. [14]
TSI	ASI	18.96	51.45
	SKIPP'D	29.07	62.91
ASI	TSI	14.91	27.71
	SKIPP'D	26.41	40.25

Table 8: Nowcasting Performance with 3 weeks training

Trained on	Finetuned on	SPIRIT	Gao et al. [14]
TSI	ASI	16.52	50.38
	SKIPP'D	27.42	62.05
ASI	TSI	14.59	27.53
	SKIPP'D	25.68	39.89

C.2 Forecasting

We conducted a series of experiments to assess the impact of training data size on model performance during fine-tuning. We utilized training splits of 2, 4, 8, 12, and 16 weeks of data at the new site. For each training duration, we performed experiments with different random splits of the corresponding number of weeks and reported the results accordingly.

Table 11: Forecasting Performance with 4 weeks of training.

Interval		Trained on	Tested on	SPIRIT	Gao et al. [14]
1hr	TSI	ASI		22.17	29.03
		SKIPP'D		32.44	39.82
	ASI	TSI		27.65	35.77
		SKIPP'D		26.54	30.70
2hr	TSI	ASI		25.13	32.69
		SKIPP'D		29.56	40.21
	ASI	TSI		31.06	36.62
		SKIPP'D		25.53	33.63
3hr	TSI	ASI		30.12	38.64
		SKIPP'D		31.79	40.18
	ASI	TSI		34.47	38.76
		SKIPP'D		29.73	39.70
4hr	TSI	ASI		36.14	41.92
		SKIPP'D		37.24	41.31
	ASI	TSI		39.72	40.02
		SKIPP'D		36.67	44.16

Table 12: Forecasting Performance with 8 weeks of training.

Interval		Trained on	Tested on	SPIRIT	Gao et al. [14]
1hr	TSI	ASI		22.62	32.45
		SKIPP'D		33.56	36.94
	ASI	TSI		26.38	35.70
		SKIPP'D		26.61	31.25
2hr	TSI	ASI		25.15	33.58
		SKIPP'D		30.65	38.06
	ASI	TSI		26.68	35.26
		SKIPP'D		25.30	33.95
3hr	TSI	ASI		28.66	35.57
		SKIPP'D		32.64	39.29
	ASI	TSI		29.81	36.44
		SKIPP'D		29.25	39.85
4hr	TSI	ASI		34.76	39.41
		SKIPP'D		37.80	41.63
	ASI	TSI		34.97	38.23
		SKIPP'D		36.23	44.25

Table 13: Forecasting Performance with 12 weeks of training.

Interval		Trained on	Tested on	SPIRIT	Gao et al. [14]
1hr	TSI	ASI		22.03	34.63
		SKIPP'D		33.76	37.35
	ASI	TSI		24.87	35.24
		SKIPP'D		28.28	31.20
2hr	TSI	ASI		24.95	35.81
		SKIPP'D		30.38	38.16
	ASI	TSI		27.42	35.31
		SKIPP'D		26.17	35.01
3hr	TSI	ASI		29.86	38.02
		SKIPP'D		31.80	39.12
	ASI	TSI		30.04	36.61
		SKIPP'D		29.61	41.13
4hr	TSI	ASI		34.37	41.27
		SKIPP'D		36.60	41.34
	ASI	TSI		35.71	38.67
		SKIPP'D		36.16	45.28

Table 14: Forecasting Performance with 16 weeks of training.

Interval		Trained on	Tested on	SPIRIT	Gao et al. [14]
1hr	TSI	ASI		22.76	28.97
		SKIPP'D		33.12	36.93
	ASI	TSI		23.33	35.07
		SKIPP'D		25.74	31.01
2hr	TSI	ASI		25.30	31.55
		SKIPP'D		30.75	38.18
	ASI	TSI		27.48	36.57
		SKIPP'D		25.83	32.22
3hr	TSI	ASI		28.86	36.28
		SKIPP'D		33.10	39.83
	ASI	TSI		31.92	39.46
		SKIPP'D		31.04	37.69
4hr	TSI	ASI		33.99	41.36
		SKIPP'D		38.20	42.66
	ASI	TSI		37.50	42.14
		SKIPP'D		38.25	42.46

Table 9: Nowcasting Performance with 4 weeks training

Trained on	Finetuned on	SPIRIT	Gao et al. [14]
TSI	ASI	15.63	50.01
	SKIPP'D	26.51	61.17
ASI	TSI	14.12	27.28
	SKIPP'D	24.32	39.43

Table 10: Forecasting Performance with 2 weeks of training.

Interval		Trained on	Tested on	SPIRIT	Gao et al. [14]
1hr	TSI	ASI		31.15	33.86
		SKIPP'D		32.35	38.24
	ASI	TSI		24.47	36.18
		SKIPP'D		27.00	30.48
2hr	TSI	ASI		32.70	36.44
		SKIPP'D		29.41	39.06
	ASI	TSI		25.93	36.71
		SKIPP'D		25.96	33.55
3hr	TSI	ASI		34.41	38.24
		SKIPP'D		31.53	39.84
	ASI	TSI		30.45	41.46
		SKIPP'D		30.03	39.76
4hr	TSI	ASI		38.19	43.76
		SKIPP'D		36.83	41.76
	ASI	TSI		36.44	45.89
		SKIPP'D		36.84	44.16

The results are presented in Tables 10, 11, 12, 13, and 14. Figure 3 was constructed by systematically aggregating the results from our fine-tuning experiments, encapsulating the performance trends observed across different training durations. By leveraging visualization techniques, the figure provides a holistic representation of how the model adapts as more site-specific data becomes available. It effectively summarizes variations in performance across different random splits of training data and across different sets of source and target datasets.

We employed 95% confidence intervals for all experiments, spanning diverse transfer learning settings and random sampling of the fine-tuning data. To rigorously compare our method with the baseline across different weekly intervals, we applied a paired t-test at a significance level of 0.001 (i.e., less than a 0.1% chance of incorrectly rejecting the null hypothesis). In every instance, the observed p-values fell below this threshold, demonstrating that SPIRIT achieves statistically significant performance improvements over the baseline.

Received 10 February 2025